Prediction of Macrosegregation in Steel Ingots: Influence of the Motion and the Morphology of Equiaxed Grains

HERVÉ COMBEAU, MIHA ZALOŽNIK, STÉPHANE HANS, and PIERRE EMMANUEL RICHY

Although a significant amount of work has already been devoted to the prediction of macrosegregation in steel ingots, most models considered the solid phase as fixed. As a result, it was not possible to correctly predict the macrosegregation in the center of the product. It is generally suspected that the motion of the equiaxed grains is responsible for this macrosegregation. A multiphase and multiscale model that describes the evolution of the morphology of the equiaxed crystals and their motion is presented. The model was used to simulate the solidification of a 3.3-ton steel ingot. Computations that take into account the motion of dendritic and globular grains and computations with a fixed solid phase were performed, and the solidification and macrosegregation formation due to the grain motion and flow of interdendritic liquid were analyzed. The predicted macrosegregation patterns are compared to the experimental results. Most important, it is demonstrated that it is essential to consider the grain morphology, in order to properly model the influence of grain motion on macrosegregation. Further, due to increased computing power, the presented computations could be performed using finer computational grids than was possible in previous studies; this made possible the prediction of mesosegregations, notably A segregates.

DOI: 10.1007/s11663-008-9178-y

I. INTRODUCTION

ONE of the major goals of the steel industry is the manufacture of products with a minimum number of defects; an important parameter of this is chemical homogeneity. Despite good control of the steel grade and chemical homogeneity of liquid steel, chemical heterogeneities develop during the solidification stage. They can be classified into three types, depending on their scale:

(1) at the dendrite scale: microsegregation, due to the difference in the solubility of chemical species in the solid and liquid phases;
(2) at the scale of the product: macrosegregation, due to the relative motion of the solid and liquid phases; and
(3) at an intermediate scale: mesosegregations (*e.g.*, A segregates, freckles), due to localized flow phenomena.

The typical segregation pattern of a steel ingot[1,2] generally consists of a negative segregation in the bottom part of the ingot and a positive in the top part. Moreover, depending on the steel grade and the size and shape of the ingot, A segregates can be observed; these correspond to highly segregated channels a few millimeters in diameter. In the center of the product, V segregates, another type of mesosegregate, can be encountered. The main phenomena responsible for these macrosegregations and mesosegregations were identified a long time ago (for example, in Reference 1): the shrinkage, the thermal and solutal natural convection of the liquid, and the motion of the equiaxed grains. The importance of each of these phenomena was not known, however, and a first generation of models appeared with the aim of estimating the effect of one or two of these phenomena.[2–5] Mehrabian and co-workers[3] studied the combined effect of the shrinkage and the natural convection of the liquid phase, for a case in which the gravity is perpendicular to the direction of solidification. In this case, they showed that the macrosegregation pattern strongly depends on the sense of variation in the density of the interdendritic liquid vs the solid fraction. They also proposed the hypothesis that A segregates develop as the result of a flow instability that occurs at a critical flow condition. Chuang and Schwerdtfeger[4] developed a two-dimensional model that considered both the vertical motion of the solid and liquid phases in the central region of the ingot and the dynamics of the grain accumulation layer, when the grains have settled at the bottom. Their model predicted a segregation profile vs the radius in the bottom part of the ingot, which was in good agreement with the measurements;

HERVÉ COMBEAU, Professor, and MIHA ZALOŽNIK, Postdoctoral Fellow, are with the Laboratoire de Science et Génie des Matériaux et de Métallurgie (LSG2M), Ecole des Mines de Nancy, Nancy-Université, Parc de Saurupt, CS 14234, F-54042 Nancy Cedex, France. Contact e-mail: miha.zaloznik@mines.inpl-nancy.fr STÉPHANE HANS, Melting and Casting Process Development Engineer, and PIERRE EMMANUEL RICHY, Research and Development Engineer, are with Aubert & Duval, BP 1, F-63770 Les Ancizes, France.

This article is based on a presentation given at the International Symposium on Liquid Metal Processing and Casting (LMPC 2007), which occurred in September 2007 in Nancy, France.

Article published online October 21, 2008.

notably, the profile reproduced the experimentally observed tendency toward a slightly positive carbon segregation in the outer region and a more pronounced negative segregation in the central part of the ingot. The density of the nuclei was an important parameter of this model: a decrease in the number of nuclei per unit volume induced an increase in the segregation intensity, due to the higher settling velocity of the larger grains. Flemings[2] analyzed the solidification in steel ingots with the help of his theory, which explained the effect of the circulation of the interdendritic liquid on segregation. Notably, he highlighted the importance of a thermally insulating hot-top design. He showed that such a design will reduce the number of equiaxed grains and, by reducing the thermal gradient, the intensity of the segregation in the top part. Olsson and co-workers[5] characterized the segregation patterns of two ingots of different steel grades, solidified under similar conditions. The interdendritic liquid of the first steel grade had a density lower than that of the bulk liquid in the whole of the two-phase domain. The second steel grade had a density that was closer to the bulk density; however, it increased near the end of solidification. Sulfur prints revealed A segregates and V structures for the first ingot and only V structures for the second one. Moreover, the positive segregation in the top part of the first ingot was more severe. Two simple models, one accounting for the settling of equiaxed crystals and the other for the solute enrichment of the bulk due to A segregates, were developed. Their application permitted the conclusion that it was the settling of crystals that was the main phenomenon responsible for macrosegregation in the second ingot; in the first ingot, it was the combination of the two phenomena.

These models were limited in that it was necessary to track the liquid-mush and the mush-solid boundaries in order to apply specific conservation equations. Significant progress was made with the development of macroscopic conservation equations that are identical for the liquid, mushy, and solid zones. These macroscopic conservation equations have been derived using a mixture theory[6] or a volume averaging procedure.[7–9] The two approaches can lead to similar equations. The main advantage of these approaches is that it is not necessary to track the different boundaries (liquid-mush, mush-solid), because there is only one conservation equation, valid for the whole domain, to be solved for each conserved quantity. The first attempts to model the formation of macrosegregations in steel ingots with these types of models accounted only for the motion of the liquid phase. Ohnaka[10] developed such a model that dealt only the case of a binary alloy. In the case of industrial alloys, a model restricted to a binary alloy may be insufficient. This is due to the fact that the variations in the liquid density are the main driving force for the liquid motion: natural convection. Since the density of the liquid changes with the temperature and composition, it is important to be able to model the solidification of a multicomponent alloy. Combeau and co-workers[11–14] proposed a slightly different approach for dealing with multicomponent alloys. They developed a model that accounted for the presence of several alloying elements. This model was of the same type as the one already proposed for a binary alloy.[7–9] It included a supplementary simplification, however: the transport of solutes was not fully coupled with the other transport phenomena. Comparison of the predicted carbon composition pattern obtained from this simplified model with those resulting from a similar but fully coupled model showed good agreement between the two calculations, in the case of a 6.2-ton ingot of a binary Fe-C alloy.[13] A good qualitative agreement between the measurements and the numerical results was also found for the same ingot;[14] eight solute elements were accounted for. The model was able to predict a negative macrosegregation at the bottom of the ingot and a positive at the top, in good agreement with the measured values. The main discrepancies were observed in the central part of the ingot, where a positive segregation was predicted, even though a negative was measured. The same conclusions were drawn in the case of a 65-ton ingot.[13] A parametric study on the effect of the diameter and the steel grade showed that the model was able to reproduce the same sensitivity to these parameters as did a statistical correlation obtained by a compilation of experimental results:[15] an increase in the ingot diameter induces an increase in both the intensity of the segregation and the content of the molybdenum, until a certain amount decreases the level of segregation by reducing the variation in the liquid density. Gu and Beckermann[16] computed the solidification of a 43-ton ingot (~1-m wide × 2-m deep × 2.8-m high), using a fully coupled model. The solid phase was assumed to be fixed; the shrinkage was taken into account, including the computation of the hot pipe. Eleven solute elements were accounted for in the computation. It is interesting to note that the data of the steel alloy showed that the density of the liquid increases during the solidification, because the enrichment of the liquid in carbon does not compensate for the temperature decrease. A grid of 38 × 54 CVs was used in the simulation reported in the article; the total CPU time mentioned by the authors was on the order of several weeks. Due to this limitation, the prediction of A segregates was out of the scope of their work. The predicted level of segregation along the vertical centerline was in good agreement with the measured values in the bottom and top regions. However, in the bottom half of the ingot, a positive segregation was predicted, while a negative one was measured. The authors attributed this difference to the neglecting of the settling of equiaxed grains.

A common conclusion of the studies reported here was that the discrepancy observed between the experiment and the model related to the central part of the ingots could be attributed to the fact that the motion of equiaxed grains was not accounted for. Beckermann and co-workers[9,17] were the first to publish multiphase models that include grain motion during solidification. The most refined model allowed the prediction of the grain morphology (dendritic or globular), the grain size, and the macrosegregation induced by the motion of the grains and the interdendritic liquid.[17] If numerical studies have been performed, these models have been compared with the experiments only a few times.

Settling experiments,[18–21] in which one grain was followed during its settling in an undercooled liquid, were used to validate some aspects of these models. Appolaire and Combeau[22] developed a one-dimensional multiscale model based on this approach, to study the macrosegregation in the central part of an ingot. The system they considered was a cylinder. New grains were injected at the vertical side of the boundary. These grains were supposed to represent fragments of columnar dendrites that penetrate into the central part of the ingot. They applied the model to a 65-ton ingot. A parametric study on the effect of the number of fragments injected into the domain showed that this number plays an important role in grain morphology and macrosegregation intensity. Notably, they showed that the higher the flux density of fragments, the lower the level of macrosegregation. The model has been able to reproduce the segregation profile along the vertical centerline of the ingot and the morphology of the grains.

In this article, a recently developed multiphase and multiscale model[23] is used to simulate the casting of a steel ingot. The model tackles the morphology evolution of the equiaxed grains and their motion, and also accounts for the flow of the interdendritic liquid in the region in which the grains are packed and motion of the grains is blocked. First, we present the experimental results of a 3.3-ton ingot cast by Aubert & Duval (Les Ancizes, France). The results obtained when two possible assumptions on the motion of solids (a fixed solid phase or moving grains) were used are presented and are compared to the measurements. As a result of the evolution of computing power, it has been possible to carry out computations on grids finer than those in the previous studies; therefore, the differences between this study and previous studies are also discussed. Finally, the influence of the grain morphology on macrosegregation is discussed. It must be pointed out that the goal of this work is not to precisely fit the results of the model with the experiment, but to show the qualitative impact of the transport and the morphology of equiaxed grains on macrosegregation.

II. EXPERIMENTAL RESULTS

A forging ingot was cast by Aubert & Duval in the steel plant of Les Ancizes, France.[24] The characteristics and the dimensions of the ingot are shown in Figure 1(a); the steel grade is reported in Table I. The ingot was a 3.3-ton octagonal ingot 2 m in height and 0.6 m in mean width. The cast-iron mold had a 10-cm-thick wall and was slightly conical, such that the ingot was 0.53-m wide at the bottom and 0.68-m below the hot top. The ingot was poured from the bottom and was cast with a hot top made of a 7-cm-thick cast-iron housing and a 3-cm-thick layer of refractory material at the inside. A 3-cm-thick layer of exothermic powder was applied at the top. The liquidus temperature of the steel was 1495 °C and the pouring superheat was 30 °C. The mold filling time was 466 seconds. The total solidification time was on the order of 90 minutes.

A carbon segregation map for a longitudinal section was measured by chemical analysis in 114 points. The locations of these points are shown in Figure 1(c), in which a concentration contour map is constructed from these points by interpolation. Note that the contour map includes regions in which there were no measurement points; as a result, the map should be used cautiously. We observe a pronounced negative segregation at the bottom of the ingot and a strong positive one in the hot top, while the carbon concentration is close to

Table I. Steel Grade of the 3.3-Ton Ingot

Alloy Element	C	Si	Mn	Ni	Cr	Mo	V
C (wt pct)	0.36	0.33	0.37	3.80	1.70	0.30	0.06

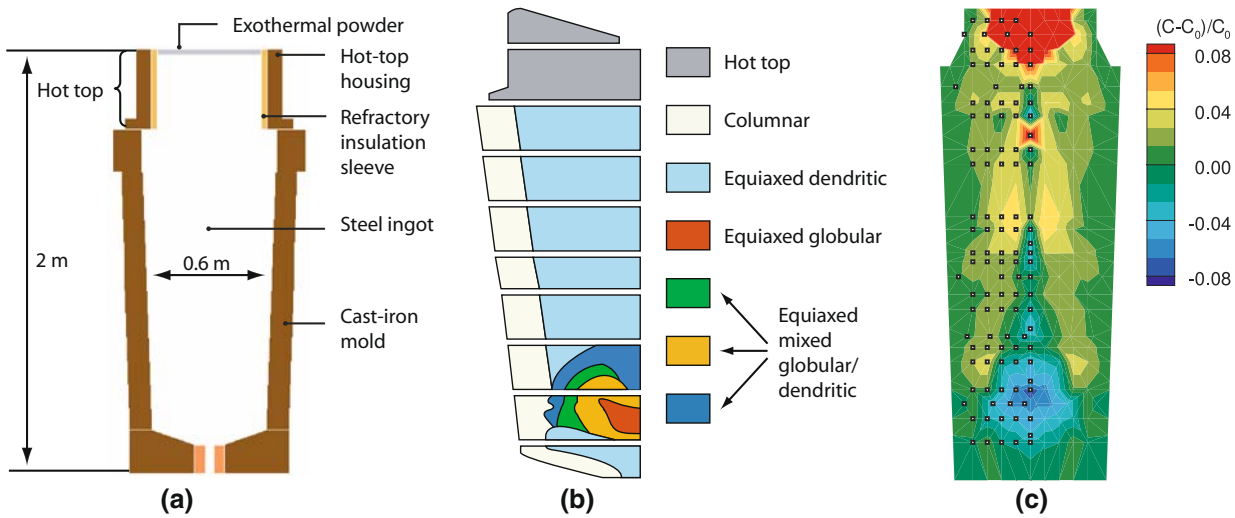

Fig. 1—Characteristics of the 3.3-ton steel ingot: (*a*) ingot and mold dimensions, (*b*) grain morphology in the ingot, and (*c*) segregation map and measurement points.

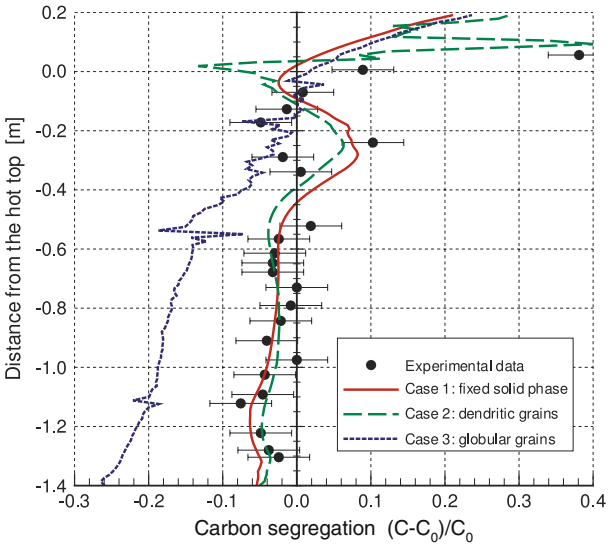

Fig. 2—Segregation ratio in carbon along the centerline of the ingot; experimental and model results.

the initial concentration in the central part of the product. Along the centerline, we can see an oscillating concentration profile (Figure 2), negative at the bottom, rising to approximately the nominal concentration at approximately one-third of the ingot height, and passing several times from negative to positive in the upward direction, until it reaches the strongly positively segregated hot top. While the centerline in the central part of the ingot tends to be negatively segregated, we can see conically shaped positive areas and strong positive spots immediately adjacent to the centerline. A positive region also surrounds the negative zone at the ingot bottom. Finer segregation structures, *i.e.*, meso-segregations such as A segregates, for example, were not observed in the test ingot. For the present steel grade, A segregates are not observed in the usual production; however, for very segregation-sensitive steel grades, the top part of the ingot would be more susceptible to the formation of this kind of defect.

Further, a macrostructure map of a longitudinal section of the ingot was made; it revealed a columnar zone with a mean width of 6 cm along the vertical ingot surface, followed by an equiaxed dendritic zone. In the equiaxed zone, the grain size increases in the upward direction. The grain morphology was clearly dendritic in most parts of the ingot, except at the bottom, where zones of globular and mixed dendritic and globular grains were found (Figure 1(b)). The secondary dendrite arm spacing (SDAS) was estimated using an intercept method and was found to evolve from 100 μm at the bottom to 800 μm at the top of the ingot.

III. MODEL

The software SOLID,[14,25] (SOLID is a casting simulation software developed by LSG2M, Nancy, France and by Sciences Computers Consultants, Saint-Étienne, France) was used for this study. The SOLID software is based on a volume-averaged Euler–Euler two-phase model that consists of two parts:[26] a macroscopic part with momentum, mass, heat, solute mass, and grain-population conservation equations, and a microscopic part that describes both the nucleation and growth of globular or dendritic grains and the phase change. The complete set of equations of the model is reported in Table II. The aim of this article is not to describe in detail the model, which is very similar to the Beckermann's model.[9,17,27] it is the principle of the model that is presented, and the original points are emphasized.

At the macroscopic level, the model accounts for the heat and solute transport, coupled with the flow driven by thermal and solutal buoyancy; solidification shrinkage is not taken into account. Depending on the behavior of the solid phase, we consider two flow regimes. The regime considered depends on the local volume fraction of the grains, g_{env}, which is defined as the ratio of the volume of grain envelopes and the total averaging volume. For dendritic grains, g_{env} is different from the solid fraction g_s (Figure 3). If the local volume fraction of the grains is larger than the packing limit ($g_{env} > g^{\text{block}}$) the solid phase in the mushy zone is considered to be blocked or coalesced, and the flow of interdendritic liquid through the porous solid matrix is described by a momentum equation, including a Darcy term used to model the drag interactions. The permeability of the porous matrix is modeled by the Kozeny–Carman law, depending on a microstructural dimension: the secondary dendrite arm spacing (SDAS). At grain-volume fractions smaller than the packing limit ($g_{env} < g^{\text{block}}$), the solid phase is considered to be in the form of free-floating equiaxed grains; the motion of the grains is described by transport equations for the solid phase. The macroscopic transport equations are derived from local continuum equations, using a volume averaging technique. Two phases, solid and liquid, are considered separately in the model (hence, this is a two-phase model); each phase is described with an Eulerian approach. In this way, the behavior of a population of grains is locally described by the behavior of an averaged grain.

The microscopic level is treated locally; within SOLID, which is based on the finite-volume method, this means that the microscopic level is treated within each control volume (CV). The formation of new grains by nucleation is modeled by an instantaneous uniform-volume nucleation law. Locally, a predefined number of spherical nuclei N_0 (density per unit volume) with a predefined initial diameter d_0 is activated when the temperature drops below the local liquidus temperature both for the first time and every time the local grain density (in the CV) becomes zero (all the grains are swept away by the flow) and the temperature is below the liquidus. The first condition ensures the nucleation of grains in every CV, even when the CV already contains grains that were transported from elsewhere. The second condition ensures the solidification of CVs that are emptied of grains by transport. In the present work, the second condition for "renucleation" is activated only at the top end of the ingot, which can be

Table II. Complete Set of Model Equations

Averaged Conservation Equations		
Averaged total mass balance	$\frac{\partial}{\partial t}(\rho_s g_s + \rho_l g_l) + \nabla \cdot (\rho_s g_s \vec{v}_s + \rho_l g_l \vec{v}_l) = 0$	[1]
Averaged mass balance of solid phase	$\frac{\partial}{\partial t}(\rho_s g_s) + \nabla \cdot (\rho_s g_s \vec{v}_s) = \Gamma_s + \Phi_s$	[2]
Averaged total heat balance	$\frac{\partial}{\partial t}(\rho_s g_s h_s + \rho_l g_l h_l) + \nabla \cdot (\rho_s g_s h_s \vec{v}_s + \rho_l g_l h_l \vec{v}_l) = \nabla \cdot (k_m \nabla(T))$	[3]
Averaged solute mass balance for the solid phase	$\frac{\partial}{\partial t}(\rho_s g_s C_s) + \nabla \cdot (\rho_s g_s C_s \vec{v}_s) = \Gamma_s C_s^* + \frac{S_V \rho_s D_s}{\delta_s}(C_s^* - C_s) + \Phi_s k_p C_l$	[4]
Averaged solute mass balance for the liquid phase	$\frac{\partial}{\partial t}(\rho_l g_l C_l) + \nabla \cdot (\rho_l g_l C_l \vec{v}_l) = \Gamma_l C_l^* + \frac{S_V \rho_l D_l}{\delta_l}(C_l^* - C_l) - \Phi_s k_p C_l$	[5]
Grain-population balance	$\frac{\partial}{\partial t}(N) + \nabla \cdot (N \vec{v}_s) = \dot{N}^{\Phi}$	[6]
Averaged grain-envelope volume balance	$\frac{\partial}{\partial t}(g_{env}) + \nabla \cdot (g_{env} \vec{v}_s) = \Gamma_{env} + \frac{1}{\rho_s}\Phi_s$	[7]
Slurry flow regime ($g_{env} < g^{\text{block}}$)		
Averaged total (solid + liquid) momentum balance	$\frac{\partial}{\partial t}(\rho_l g_l \vec{v}_l) + \nabla \cdot (\rho_l g_l \vec{v}_l \vec{v}_l) = \nabla \cdot (\mu_l \nabla(g_l \vec{v}_l)) - \nabla p + \rho_m^b \vec{g}$	[8]
Explicit expression for the velocity of the solid phase	$\vec{v}_s = \vec{v}_l + \frac{4 d_g^2 (1 - g_{env})}{3 C_d \mu_l \text{Re}}\left(-\nabla p + \rho_g^b \vec{g}\right)$	[9]
Densities in the buoyancy terms:	$\rho_m = \rho_s g_s + \rho_l (1 - g_s)$ and $\rho_g = \rho_s g_i + \rho_l (1 - g_i)$ $\rho_l^b = \rho_{ref}[1 + \beta_r (T - T_{ref}) + \beta_c (C_l - C_{ref})]$, $\rho_m^b = \rho_s^b g_s + \rho_l^b (1 - g_s)$, $\rho_g^b = \rho_s^b g_{si} + \rho_l^b (1 - g_{si})$	[10]
	$\text{Re} = \frac{\rho_l d_g (1 - g_{env}) \lvert \vec{v}_s - \vec{v}_l \rvert}{\mu_l}$	[11]
	$C_d = \frac{48 C_{ke}(1 - g_l)}{\text{Re}} + C_{ie}$	[12]
If $g_{env} \le 0.5$:	$C_{ke} = \frac{25}{6}$, $C_{ie} = \frac{7}{3}$	
If $g_{env} > 0.5$:	$C_{ke} = \frac{1}{2}\frac{(1 - g_{env})^3}{g_{env}}\frac{1 + 4.7 g_{env}}{1 + 1.83 g_{env}}$, $C_{ie} = \frac{24(10^E - 1)}{Re\left[1 - 0.9(0.75 - g_{env})^{1/3} g_{env}^{2/3}\right]^3}$	[13]
	$E = 0.261\text{Re}^{0.369} - 0.105\text{Re}^{0.431} - \frac{0.124}{1 + (\log_{10} \text{Re})^2}$	
Porous flow regime ($g_{env} \ge g^{\text{block}}$)		
Average liquid momentum balance	$\frac{\partial}{\partial t}(\rho_l g_l \vec{v}_l) + \nabla \cdot (\rho_l g_l \vec{v}_l \vec{v}_l) = \nabla \cdot (\mu_l \nabla(g_l \vec{v}_l)) - g_l \nabla p - \frac{g_l^2 \mu_l}{K}\vec{v}_l + \rho_l^b g_l \vec{g}$	[14]
Permeability	$K = \frac{\text{SDAS}^2}{20\pi^2}\frac{g_l^3}{(1 - g_l)^2}$	[15]
Nucleation		
If at time t_0, $(T < T_f + m_L C_l)$ and $\left(\int_0^{t_0} \dot{N}^{\Phi} dt = 0 \text{ or } N = 0\right)$:	$\dot{N}^{\Phi} = N_0 \delta(t - t_0)$, where δ is the Dirac function,	
else:	$\dot{N}^{\Phi} = 0$	[16]
Solid mass generation due to nucleation:	$\Phi_s = \rho_s V_0 \dot{N}_0$	[17]
Grain Growth Kinetics		
Growth rate of the averaged grain-envelope volume The tip velocity V_{tip} is computed by the Kurz-Giovanola-Trivedi (KGT) model.[31]	$\Gamma_{env} = \frac{1}{\sqrt{3}} S_{env} V_{\text{tip}}$	[18]
Averaged mass balance at the solid-liquid interfaces	$\Gamma_s + \Gamma_l = 0$	[19]
Averaged solute balance at the solid-liquid interfaces	$\Gamma_s (C_l^* - C_s^*) = \frac{S_v \rho_l D_l}{\delta_l}(C_l^* - C_l) + \frac{S_v \rho_s D_s}{\delta_s}(C_s^* - C_s)$	[20]
Diffusion lengths	$\delta_l = \frac{d_s}{2}\left[\frac{1}{1 - (1 - g_l)^{1/3}} + \frac{\text{Sc}^{1/3}\overline{\text{Re}}^{\alpha}}{3 g_l}\right]^{-1}$,	[21]
	where $\text{Sc} = \frac{\mu_l}{\rho_l D_l}$, $\alpha = \frac{2\overline{\text{Re}}^{0.28} + 4.65}{3\left(\overline{\text{Re}}^{0.28} + 4.65\right)}$; $\overline{\text{Re}} = \frac{\rho_l d_s g_l \lvert \vec{v}_s - \vec{v}_l \rvert}{\mu_l}$	
	$\delta_s = \frac{d_s}{10}$	[22]
Relations for the thermodynamic equilibrium at the solid-liquid interfaces	$C_s^* = k_p C_l^*$	[23]
	$T = T_f + m_L C_l^*$	[24]
Geometric Relations		
Volume of a grain	$V_{env} = \frac{4}{3} l_1^3$	[25]
Diameter of a sphere that has the same volume as the grain	$d_g = \frac{2}{\sqrt[3]{\pi}} l_1$	[26]
Diameter of a sphere that occupies the same volume as the solid phase within the grain	$d_s = \left(\frac{3 g_s}{4\pi N}\right)^{1/3}$	[27]
Specific surface area of the grain envelopes	$S_{env} = N\sqrt{3}\pi^{2/3} d_g^2$	[28]

Specific surface area of the liquid/solid interfaces
if $g_s < g_s^c$:
if $g_s \ge g_s^c$:
	$S_V = N\pi d_s^2$
	$S_V = N\pi d_s^2 \left(\frac{g_s}{g_s^c}\right)^{1/3}\left(\frac{1 - g_s}{1 - g_s^c}\right)^{\frac{1 - g_s^c}{g_s^c}}$
		[29]

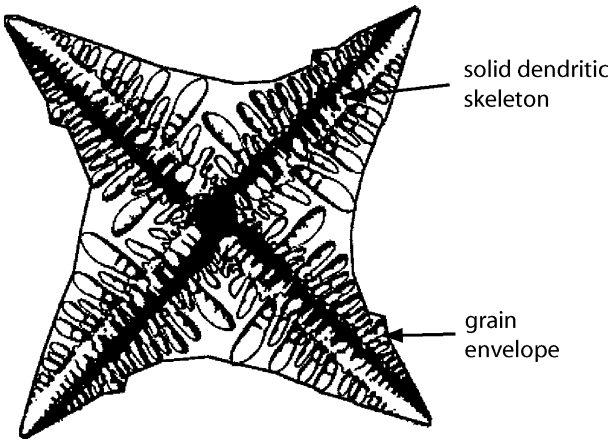

Fig. 3—Representation of a grain by an envelope containing a solid skeleton and an interdendritic liquid.

emptied due to grain settling. Other types of nucleation laws, uniform and nonuniform, were also investigated.[28,29]

At the microscopic level, we further model phase change (solidification and melting) and grain growth. A dendritic grain is defined by an envelope,[30] which links the tips of the primary and secondary dendrite arms, as shown in Figure 3. A solid skeleton and an interdendritic liquid are present inside this envelope. The interdendritic liquid is not considered a separate phase, as, for example, in Reference 17, but is simplified as being identical to the bulk extradendritic liquid. The internal solid fraction, defined as the ratio of the volume occupied by the solid phase in the grain and the volume of the envelope of the grain ($g_{si} = g_s/g_{env}$), is the parameter by which the grain morphology is described. A value of the internal solid fraction close to 1 indicates that the morphology of the grain is globular, while a value close to 0 indicates a dendritic morphology. The envelope is assumed to be of a regular octahedral shape, which corresponds to the assumption that the tip velocities of the primary and secondary dendrite arms are equal. The envelope growth is deduced from the calculation of the tip velocity by the Kurz-Giovanola-Trivedi (KGT) model,[31] if the grain morphology is dendritic. The phase change inside the envelope is controlled by solute diffusion in both phases on the secondary dendrite arm scale, assuming local thermal equilibrium and thermodynamic equilibrium at the solid-liquid interface. The morphology of a grain is determined by g_{si}, which follows from the competition between the envelope growth and the solidification inside the envelope. Apart from the dendritic model, it is possible to use a simpler globular grain model in SOLID. In this case, the grains are considered spherical; the envelope thus matches the solid liquid interface and the internal solid fraction is equal to one. In this case, the phase change is considered at the scale of the grain.

To describe the transport of grains in the free-floating regime, a momentum equation for the solid phase has been derived. The motion of the grains is governed by a balance of buoyancy, drag, and pressure forces. In this way, the solid and liquid phases have locally different velocities. In particular, on the one hand, the density of the solid phase is higher than that of the liquid; on the other hand, the interfacial particle drag is considered dependent on the grain (*i.e.*, envelope) size. This produces the phenomenon that the more globular and larger the grains, the stronger their tendency to settle; contrarily, smaller and more dendritic grains are more easily entrained by the liquid motion.

In this way, we can predict the composition, grain density, and grain morphology in the solidified casting with SOLID. The grain morphology is defined by the internal solid fraction at the instant at which the grains are blocked.

The SOLID software implements a finite-volume method with a first-order upwind interpolation for convection and a second-order centered scheme for diffusion, to solve the convection-diffusion transport equations. It employs an operator-splitting scheme, to split the macroscopic transport terms and the microscopic phase-change and nucleation terms of the conservation equations. The resolution of the velocity-pressure coupling is performed by the SIMPLEC (semi-implicit method for pressure-linked equations-consistent) algorithm, employing staggered grids for the velocities. The linear systems of the discretized equations are solved by an alternating-direction-implicit tridiagonal-matrix algorithm (ADI-TDMA). For the computations in this work, a rectilinear axisymmetric mesh composed of 11,057 cells was used, 6408 cells contained in the steel ingot and the rest in the mold. This corresponds to an average cell size of approximately 7×12 mm (width $\times$ height). The mesh was refined along the steel-mold interface, to capture more precisely the inclination of the mold that we described as a staircase pattern. The time-step was variable, on the order of 0.01 seconds.

IV. NUMERICAL RESULTS AND DISCUSSION

We used SOLID to investigate the origin of the macrosegregation observed in the 3.3-ton ingot. The following three principal cases were investigated, to study the effect of grain motion and morphology on the macrosegregation in the ingot.

(a) Case 1: the solid phase is fixed everywhere ($g^{\text{block}} = 0$). This roughly corresponds to a classical model, with the notable exception that the solute diffusion model is used to describe the phase-change kinetics.
(b) Case 2: for free-floating grains with a packing limit of $g^{\text{block}} = 0.40$, the dendritic grain model was used and a dendritic grain morphology developed.
(c) Case 3: for free-floating grains with a packing limit of $g^{\text{block}} = 0.40$, the globular grain model was used, *i.e.*, a globular grain morphology was imposed.

The nucleation density was $N_0 = 10^9$ m^{-3}, in all cases. The predicted grain morphology in case 2 turned out to be clearly dendritic in the whole ingot, which does not completely agree with the structure found experimentally, in which globular and transitional regions were

Table III. Main Parameters Used in the Simulations

Initial Conditions	
Steel temperature	1503.038 °C (This value corresponds to the liquidus temperature of the model steel; no superheat is considered.)
Iron mold temperature	25 °C
Refractory material temperature	25 °C
Covering powder temperature	1500 °C
Thermal Boundary Conditions	
1. Interface between steel and mold, variable heat transfer resistance	$0.0035\ W^{-1}\ m^2\ K$ for time < 3000 s $0.0039\ W^{-1}\ m^2\ K$ for time > 3000 s
2. Interface between the iron mold and the outside, Fourier condition	$h = 7.5\ W/(m^2\ K) + 4 \cdot 5.6710^{-8}\ W/(m^2\ K^4) \cdot \varepsilon T^3$, $\varepsilon = 0.9$, $T_{ext} = 20$ °C
3. Interface between the refractory material and the outside, Fourier condition	$h = 5.0\ W/(m^2\ K) + 4 \cdot 5.6710^{-8}\ W/(m^2\ K^4) \cdot \varepsilon T^3$, $\varepsilon = 0.5$, $T_{ext} = 100$ °C
4. Contact boundary between the mold and the ground, Fourier condition	$h = 5\ W/(m^2\ K)$, $T_{ext} = 100$ °C
Alloy Properties	
Melting temperature of pure iron	1532 °C
Carbon content	0.36 wt pct
Partition coefficient	0.314
Liquidus slope	−80.45 K/wt pct
Solutal expansion coefficient	$1.4164 \cdot 10^{-2}\ (wt\ pct)^{-1}$
Thermal expansion coefficient	$1.07 \cdot 10^{-4}\ K^{-1}$
Reference density	$6990\ kg/m^3$
Latent heat	271,000 J/kg
Dynamic viscosity	0.0042 Pa · s
SDAS	500 μm
Thermal conductivity of the solid phase	25 W/(mK)
Thermal conductivity of the liquid phase	39.3 W/(mK)
Specific heat at constant pressure	500 J/(kgK)
Diffusion coefficient of carbon in the liquid	$2 \cdot 10^{-8}\ m^2/s$
Diffusion coefficient of carbon in the solid	$5.187 \cdot 10^{-11}\ m^2/s$

detected at the bottom of the ingot (Figure 1(b)). As we will show later, the grain morphology affects the significance of the grain settling with regard to the macrosegregation, with globular grains resulting in a stronger settling effect on the part of the solute-lean grains. Note that the difference between the so-called dendritic grain model, used in case 2, and the globular grain model of case 3 is that, in case 3, the globular grain morphology is imposed by the grain model; in case 2, however, the grain morphology is solved by the grain growth kinetics model. In order to account for the columnar zone that we observed experimentally, the grains were imposed to be fixed within a layer 6 cm in width, along the vertical surface of the ingot, in all cases. In the vertical direction, this layer spreads from the bottom of the ingot to just below the hot top; it is shown in Figure 1(b).

The thermophysical properties of the alloy, the boundary conditions, and the other main parameters of the model are summarized in Table III. The thermal contact resistance conditions for the mold-steel interface were obtained by an inverse method.[24] To model the steel properties, we considered a binary iron-carbon alloy with a nominal composition of $C_0 = 0.36$ wt pct C, neglecting the other alloying elements. This simplification is justified by the fact that, of all the alloy components, carbon has the strongest effect on the solutal buoyancy forces that drive the convection flow together with the thermal buoyancy. We estimated this by comparing the effects of the individual elements on the total (combined thermal and solutal) buoyancy force. For the purpose of this estimation, we consider a simplified growth model by neglecting macrosegregation, assuming a microscopic equilibrium (equivalent to the lever rule) for the carbon, and taking the Scheil assumption for the other alloy elements. In this way, we can relate the local temperature and the liquid concentration by the equilibrium relation $T = T_f + \sum m_L^i C_l^i$, which allows us to express the total (combined thermal and solutal) buoyancy force as

$$B \propto \sum_i \left(m_L^i \beta_T + \beta_C^i\right) \Delta C_l^i \qquad [1]$$

Using the aforementioned Scheil-lever solidification path, we can express the buoyancy force as a function of the liquid fraction and determine the contributions of the individual elements. This estimation procedure is similar to the one used by Schneider and Beckermann;[32] like them, we reach the conclusion that, of all the

elements, carbon exerts the strongest buoyancy force. However, in contrast to Reference 33, our thermophysical data, presented in Table II, indicate that $|m_L\beta_T| < |\beta_C|$. This means that the solutal effect of carbon dominates over the thermal effect. Because carbon has a density lower than iron, its solutal buoyancy force opposes the thermal buoyancy, *i.e.*, β_T has a negative sign and β_C has a positive sign; thus, with a dominant solutal force, we can expect an inversed flow direction (ascending along the chill).

The simplification to a binary alloy also requires a careful consideration of the solidification path. The solidification of the multicomponent steel specified in Table I starts with the formation of austenite. Therefore, we considered the solidification of our model, 0.36 pct carbon steel, as austenitic, as well, although a binary 0.36 pct carbon steel would start to solidify, with the formation of ferrite. To model this, we used the binary liquidus slope and the partition coefficient of the austenite region.

A. *Fixed Solid Phase*

The final map of carbon segregation from the simulation with a fixed solid phase (case 1) is compared with the experimental map, in Figure 4 (a), and with a centerline profile, in Figure 2. Following the centerline, the simulation predicts a strong positive segregation of carbon in the hot-top part, a negative segregation below, a positive spot at the centerline, and a transition to negative segregation in the downward direction. Off the centerline, we observe a conically shaped negative segregation zone at the bottom of the ingot that extends upward along the centerline. This is in good agreement with the measured tendencies. Next to this zone, in the central part of the ingot, we seem to observe at first glance a slight tendency toward the conically shaped positive segregations found experimentally. However, this zone is neutral to slightly negative in the simulation; only several slightly positive bands appear near the surface. Note also that there is no certainty about the continuity of the central positive bands shown on the experimental map, because there are not enough measurement points at approximately two-thirds of the ingot height, as shown in Figure 1(c). Likewise, there are not enough measurement points close to the surface to be able to judge the positive spots at the outer surface. We can say the same about the zone of strong negative segregation predicted by the model at the surface of the hot top. A striking feature of the numerical results are the predicted A segregates: strong, banded mesosegregations in the top part of the ingot. These segregations

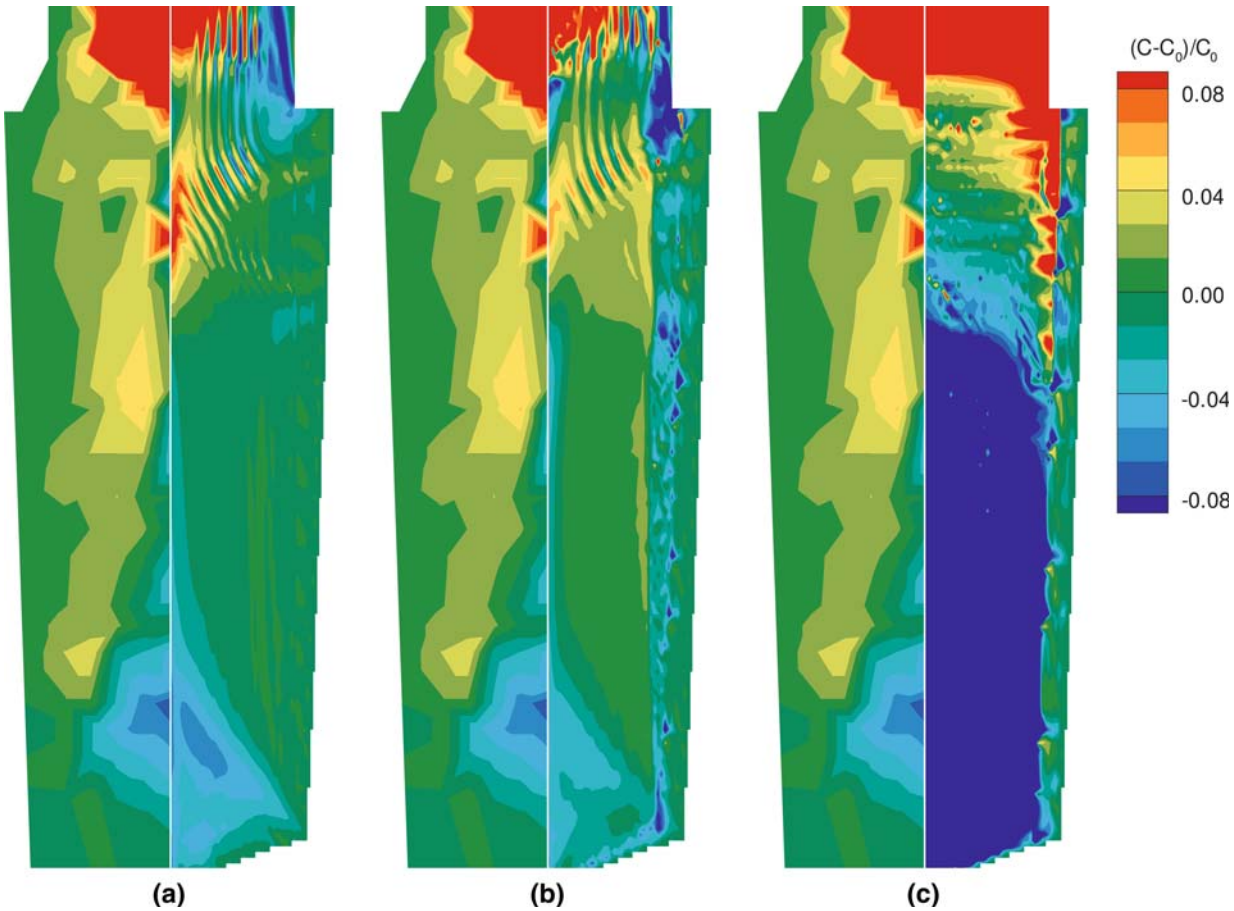

Fig. 4—Segregation ratio $(C - C_0)/C_0$ for carbon. Left: experimental results. Right: numerical simulation. (*a*) Case 1: fixed solid phase. (*b*) Case 2: dendritic free-floating grains, $N_0 = 10^9$ m^{-3}. (*c*) Case 3: globular free-floating grains, $N_0 = 10^9$ m^{-3}.

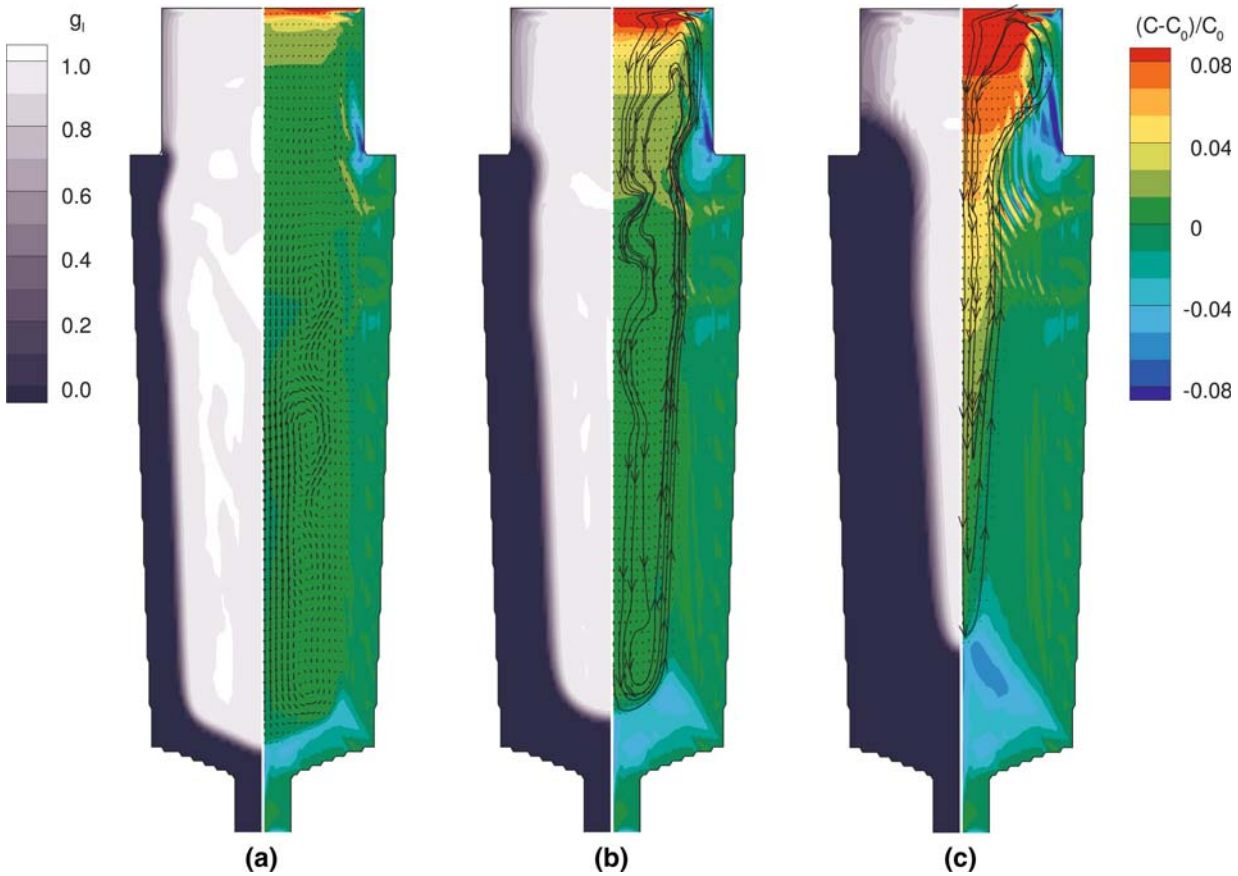

Fig. 5—Model results for a fixed solid phase (case 1). Left: solid fraction and solid velocity. Right: macrosegregation ratio and liquid velocity. (*a*) 900 s, (*b*) 1800 s, and (*c*) 3600 s.

develop as a result of instabilities in the mushy zone growth that perturb the fluid flow at the scale of a few centimeters. This relatively small scale makes it difficult to attain a spatial resolution with the model that is sufficient to capture enough detail. Indeed, this is the first time that we are able to predict mesosegregates in steel ingots. In previous work,[16] the limitations of computing resources did not permit a grid resolution sufficiently high to resolve the mesoscale structures. We observed the same effect with SOLID, with which we did not predict mesosegregates with the coarser grids used in the preceding studies.[28,29] In these studies, we had used grids with a grid spacing approximately three times larger, *i.e.*, with a mean size of approximately 23 × 30 mm, which is on the same order as the grids in Reference 16. Nonetheless, the resolution of the experimental map is not sufficient to observe A segregates. Therefore, it is presently not possible to compare the model and the experiment in this matter. In summary, the model with a fixed solid phase appears to give a fairly good prediction of segregation tendencies; the exceptions are the positive segregations in the bottom half of the ingot, which it fails to predict, and the positive hot-top segregation, which is underestimated.

The predicted evolution of both the solidification and the macrosegregation in the ingot is presented in Figure 5. Because the melt is initially not superheated, solidification starts immediately in the whole ingot; the growth kinetics controls the sensible heat release and, thus, the temperature in the ingot center. Because the latent heat release is much larger than the sensible heat transfer, the core of the ingot is kept isothermal; here, the heat transfer is controlled solutally. The small variations in temperature and liquid fraction that can be observed in the core at 900 seconds (Figure 5(a)) are induced by the solute transport in the liquid, because the kinetics of the phase change (solidification and melting) keeps the liquid close to thermodynamic equilibrium; the undercoolings are on the order of 0.1 K. After the onset of the cooling, a relatively weak thermal convection, descending at the solidification front and ascending at the centerline (hereafter termed clockwise direction), is established. The fraction of solid in the core is extremely small; therefore, no significant segregation is produced here at this moment. Later, the ingot core starts to segregate through the enriched liquid brought in from the mushy zone next to the surface, where the solidification has already advanced; the temperatures are lower and the liquid is richer in carbon. Consequently, important solutal gradients build up in the core. As already pointed out, here the liquid is kept practically at thermodynamic equilibrium by the phase-change kinetics. Thus, we can estimate the gradient of the thermal buoyancy forces as $\beta_T \nabla T \approx m_L \beta_T \nabla C_l^C$, and the total buoyancy as $(m_L \beta_T + \beta_C) \nabla C_l^C$. Because

$|m_L\beta_T|/|\beta_C| < 1$, the solutal buoyancy dominates, and the flow in the core is governed by the solute transport. In our case, the solutal forces oppose the thermal force and start to invert the initial thermally driven clockwise flow. At approximately 100 seconds, solutal plumes start to rise from the mushy zone at the bottom of the ingot. At the same time, the flow also starts to invert in the mushy zone along the outer ingot surface; while the flow in the core is still turning clockwise, the solutal buoyancy starts to drive the liquid upward at the mold side. The flow becomes destabilized here; several narrow counterclockwise-flow cells form, which create the positive segregation patches observed in the final segregation map. The flow inversion is accomplished at approximately 900 seconds, when the flow is counterclockwise everywhere, with several flow cells (Figure 5(a)). During this time, a stable solutal stratification and an inverse thermal stratification are set up in the ingot core. This situation is a result of the peculiar conditions of the thermosolutal convection. The solutal buoyancy controls the flow and creates a stable stratification, while the thermal configuration is merely a consequence of the solutal field and the equilibrium maintained by the phase-change kinetics. The buoyancy force of the thermal field, unstable by itself, is too weak to destabilize the stable solutal stratification.[33] The vertical thermal and solutal gradients change sign only at the bottom of the mushy zone, where the heat extraction is strong and the gradients of the liquid concentration are large. We observe a temperature maximum and, correspondingly, a minimum in liquid composition, just above the bottom of the liquid pool, which we can see in Figure 6 (a). Below this hot spot, the counterclockwise flow turns and the circulation brings solute-lean liquid into the mushy zone; the flow is directed in the opposite direction of the temperature gradient. As indicated by a simplified treatment described in the Appendix, the development of the segregation in the case of a fixed solid depends on the direction of the temperature gradient and the liquid flow. Eq. [A3] simplifies to

$$\frac{\partial C_m}{\partial t} = -\frac{1}{m_L} g_l \vec{v}_l \cdot \nabla T \qquad [2]$$

Eq. [2] clearly demonstrates the development of a negative segregation in the zone of liquid penetration into the mushy zone. Due to the evolution of the shape of the liquid pool, a conically shaped negative segregation zone forms at the bottom (Figures 5(b) and 6(a)). In the larger part of the ingot, above the hot spot, the circulation flows upward along the mushy zone front and parallel to the isotherms, and is, thus, more or less neutral, with respect to macrosegregation generation. At the top of the hot top, the stream leaves the mushy zone and turns back downward, moving counterclockwise. This means that, here, the flow is locally oriented in the direction of the temperature gradient and, thus, leads to a positive segregation (Eq. [2]). This shows that the origin of the positive hot-top segregation is not in the formation of A segregates, as proposed in Reference 2, but occurs simply due to the orientation of the flow, with respect to the heat-extraction direction. This is further affirmed by our coarse-grid results, which predict strongly positive segregation at the top (Figures 7 and 8), even without the formation of A segregates

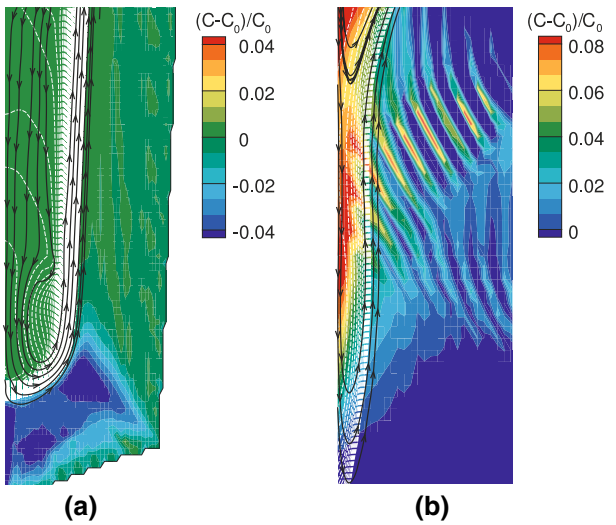

Fig. 6—Solutally driven flow in the ingot core in the case of the fixed solid (case 1) and the development of two segregation zones. The segregation field, isotherms, and liquid streamlines are shown (note the different scales for the temperature and segregation ratio). (*a*) Development of the negative segregation at the bottom. $t = 1800$ s, isotherms: $\Delta T = 0.01$ °C. (*b*) Development of the centerline segregation in the top part. $t = 4920$ s, isotherms: $\Delta T = 1$ °C.

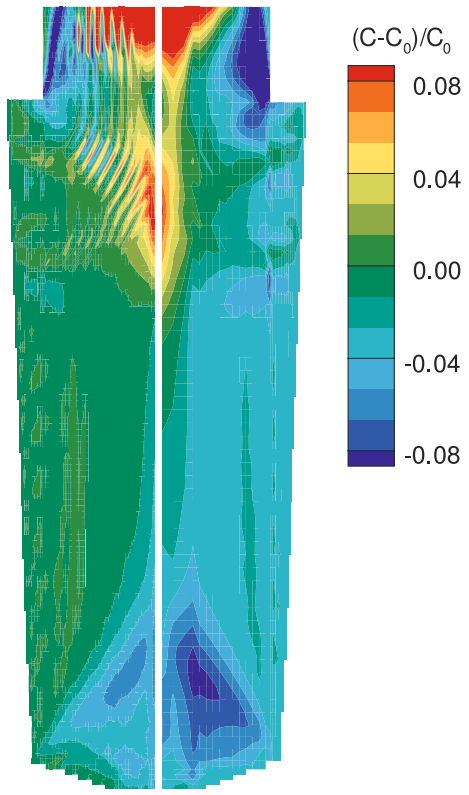

Fig. 7—Effect of the grid density on the predicted carbon macrosegregation for the fixed-solid case. Left: fine grid. Right: coarse grid.

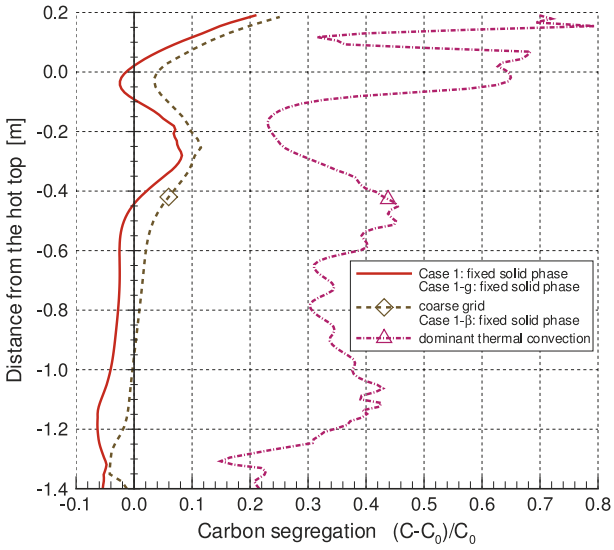

Fig. 8—Effect of the grid density and the volume expansion coefficients on the predicted carbon macrosegregation along the centerline for the fixed-solid case.

(as already explained, grids that are too coarse prevent the prediction of mesosegregates). Globally, this situation gradually develops an enrichment of the liquid in the center. The inverse thermal stratification in the center of the ingot leads to the situation in which the counterclockwise flow descending at the centerline is also oriented in the direction of the temperature gradient, down to the temperature maximum in the hot spot on the centerline. Thus, there is a positive segregation tendency at the centerline. The carbon concentration increases in the region above the hot spot. As the hot spot, which is moving upward as solidification proceeds, passes above, the very high temperature gradient below the hot spot makes the concentration drop sharply. We can observe this in Figure 11, in which the evolution of a point, located at the centerline, 1.11-m below the hot-top joint, is shown (hereafter termed point P). At the beginning, the hot spot is below point P and the composition increases, due to the local flow direction and global enrichment of the center. This continues up to the point at which the hot spot passes above point P, and a strong negative segregation tendency sets in, due to the fluid flow direction and the strong reversed temperature gradient (Eq. [2]), finally resulting in a negative segregation. Such an evolution is valid at the centerline, up to approximately two-thirds of the height. To understand the segregation profile higher up along the centerline, we have to look at the later stages of the solidification, always keeping with the interpretation by Eq. [2]. Due to the shape of the mold and the heat transfer, the isotherms in the mushy zone in the top two-thirds of the ingot have a wavy shape (Figure 5(c)). Toward the end of the solidification of the ingot, at approximately 4800 seconds, the isotherms at the centerline "close" laterally, and a second temperature maximum is set up at approximately the level of the hot-top joint. Now, the descending flow at the centerline tends to create a positive segregation above each temperature maximum and a negative below, as the sign of the scalar product of the temperature gradient and the liquid velocity in Eq. [2] changes (Figure 6(b)). This interchangeable segregation tendency at the centerline, negative-positive-negative-positive from bottom to top, explains the positive and negative segregation alterations of segregation at the centerline in the top part of the ingot (Figure 2).

The A mesosegregates in the top part of the ingot are formed in a region in which the shape of the mushy zone changes. The liquid fraction isolines that are straight in the bottom part of the ingot bend here, due to the heat transfer through the mold (Figure 5(c)). The flow is no longer aligned, but tends to leave or enter the mushy zone. At the same time, the coupled heat and solute transport, fluid flow, and solidification provoke a destabilization of the mushy zone advancement; the liquid fraction isolines become wavy, on a scale of several centimeters. The temperature field, on the other hand, is dominated by heat conduction, and stays smooth. The fluid flow adapts to the liquid fraction field, due to the large differences in hydrodynamic resistance (permeability variations). Therefore, it alternates its direction with respect to the temperature gradient; consequently, the segregation tendency varies on the scale of the channel-like structures. An oscillation between a positive and a negative segregation tendency is created at a mesoscale of several centimeters. Let us emphasize that this destabilization is not triggered by local remelting, but by a destabilization of the advancement of the mushy front.

We can see that the presented results and discussion show, as a key phenomenon, the dominance of solutal buoyancy as the driving force of the flow. This might seem controversial, in view of the preceding work of Gu and Beckermann,[16] which showed a clockwise-flow circulation dominated by thermal buoyancy. The decisive difference between the two studies is in the values of the thermal and solutal expansion coefficients. To address this issue, we performed a calculation with a modified volume expansion coefficient that implies a dominant thermal buoyancy effect, *i.e.*, $|m_L\beta_T| > |\beta_C|$, and found a completely different macrosegregation field. Although we do not elaborate on the results in detail here, we can show that, most notably, the centerline segregation is strongly positive in this case, as shown in Figure 8. This is not surprising; the clockwise flow that is maintained throughout the solidification creates a flow in the direction of the temperature gradient in the center and, using Eq. [2], as before, we can identify a positive segregation tendency. Thus, with this alternate choice of volume expansion coefficients, we could not approach the experimentally observed macrosegregation.

B. *Dendritic Free-Floating Grains*

The evolution of the ingot solidification in the presence of free-floating dendritic grains (case 2) is shown in Figure 9. Here, the solidification starts with the formation of the columnar layer at the surface. Soon, free-floating equiaxed grains start to form, first in the hot-top part, where there is no fixed columnar layer,

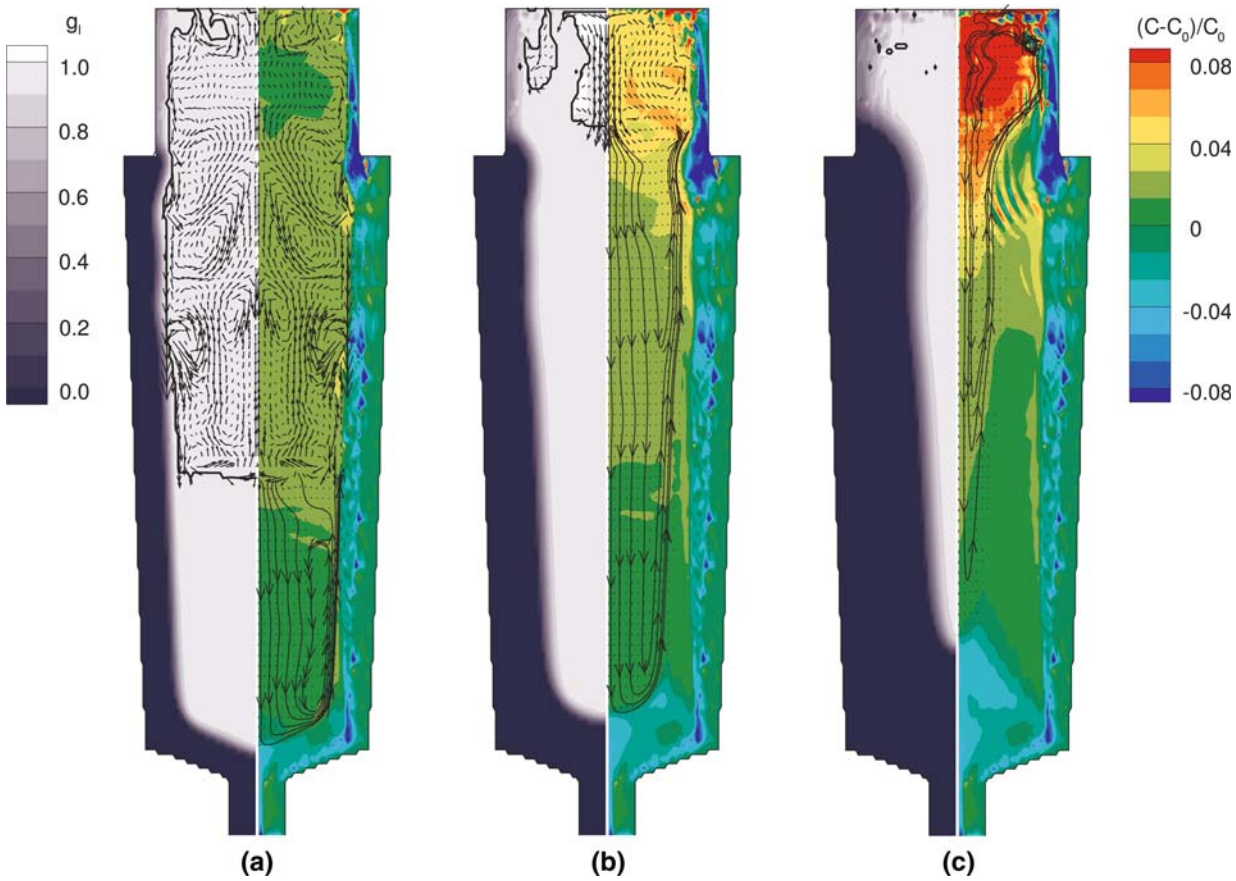

Fig. 9—Model results for free-floating grains with a predominantly dendritic morphology (case 2). Left: solid fraction, solid velocity, and coherency front (g_{env} = 0.4). Right: macrosegregation ratio and liquid velocity. (*a*) 900 s, (*b*) 1800 s, and (*c*) 3600 s.

then in front of the columnar zone. Because solid is heavier than liquid, the grains start to descend along the columnar zone and entrain the liquid to flow downward; they immediately create a strong clockwise flow in the core. The descending current also induces cells with a weaker counterclockwise flow in the fixed columnar zone, creating the negative segregation bands. As the grains settle to the bottom, they are blocked at a grain fraction of g_{env} = 0.4. The grains grow strongly dendritic, with internal solid fractions in a range between 0.01 and 0.1. Thus, they occupy a large volume (g_{env}), but carry only a small mass of solute-lean solid (g_s). In effect, the sedimenting grains quickly fill up the volume of the ingot core; on the other hand, however, their sedimentation deposes very little solid mass. In other words, the sedimentation layer has a very low solid fraction ($g_s = g_{env}g_{si}$) and the tendency toward negative segregation due to the transport of solute-lean grains, is correspondingly very weak. This can be seen in Figure 9(b); after all the grains had already been blocked, the segregation in the core is only weak. The decisive solute transport occurs later, through the interdendritic liquid flow in the packed layer (Figure 9(c)). We analyze this situation in a more lucid way in Eq. [A3] in the Appendix. Whereas the second term (grain transport) of Eq. [A3] is slightly dominant, with a negative segregation tendency during the settling phase, its cumulated effect is later surpassed by the contribution of the first term (flow of enriched liquid), as liquid circulates in the packed layer.

The importance of the grain settling is elsewhere. The permeability of the packed porous layer strongly depends on the solid fraction g_s. Although the increase in the solid fraction in the sedimentation layer is small, the corresponding decrease in the permeability is enormous. For example, at the point in the ingot centerline traced in Figure 11, the solid fraction between 1000 and 3000 seconds is 0.001 in case 1 (fixed solid) and 0.03 in the packed layer of case 2 (free-floating dendritic grains). Because the dependence of the permeability on the solid fraction is $K \sim (1 - g_s)^3/g_s^2$, this small change in the solid fraction causes the permeability to decrease by approximately 1000 times. As a result, the flow velocities in the packed layer are much smaller when the dendritic grains settle to the bottom than when they are fixed, as is shown in Figure 11. Apart from that, the flow conditions in the packed layer are equivalent to the ones we observed in the fixed-solid case. The solutal buoyancy dominates the driving force and establishes a counterclockwise flow. This creates a negative macrosegregation at the bottom and along the centerline, a positive macrosegregation in the hot top, and mesosegregations at the top of the ingot. The mechanisms of the creation of these segregations are the same as in the case

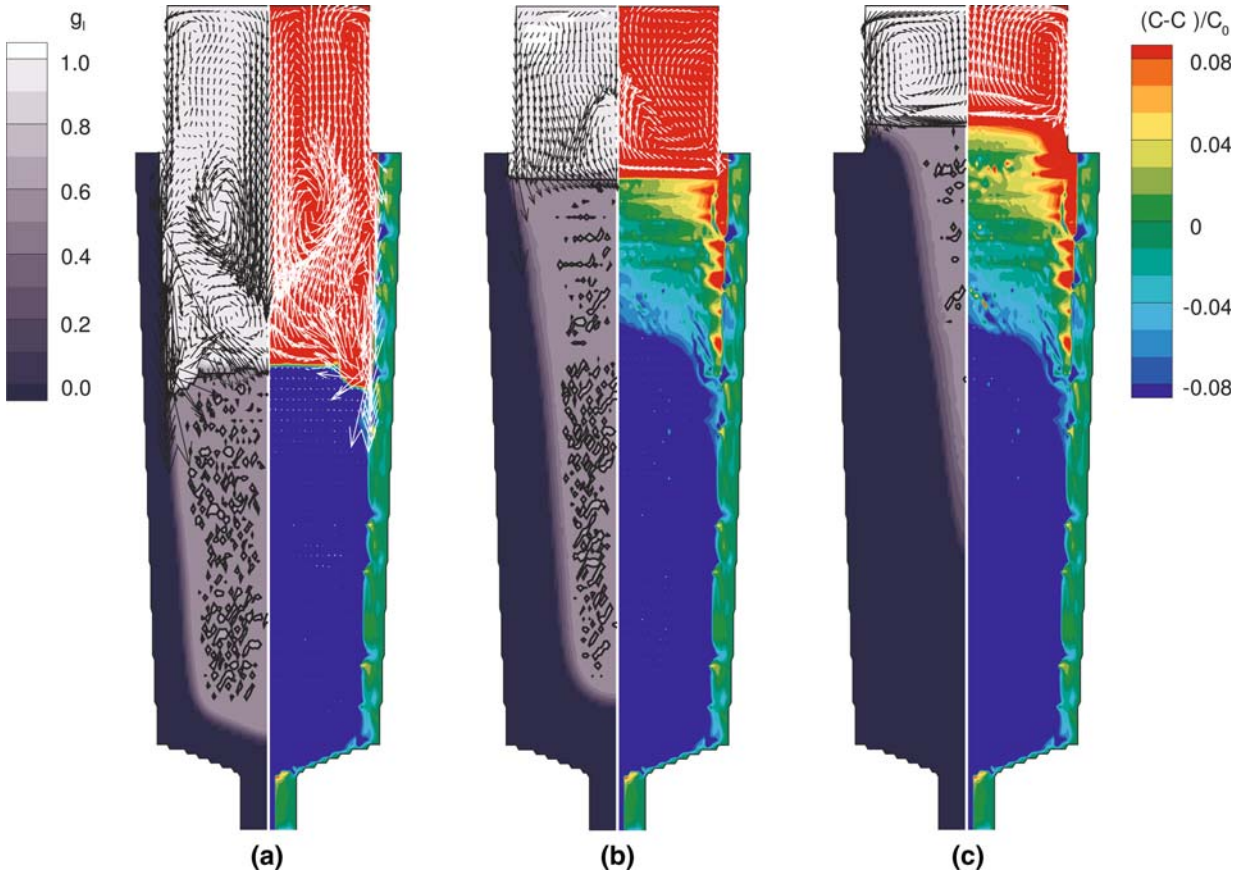

Fig. 10—Model results for free-floating globular grains (case 3). Left: solid fraction, solid velocity, and coherency front ($g_s = g_{env} = 0.4$). Right: macrosegregation ratio and liquid velocity. (*a*) 900 s, (*b*) 1800 s, and (*c*) 3600 s.

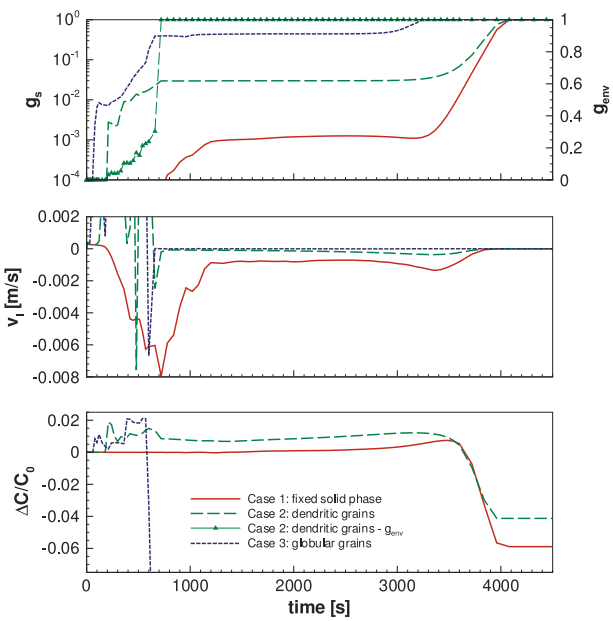

Fig. 11—Evolution of the solid fraction and grain-volume fraction (top), the vertical liquid velocity (middle), and the segregation ratio (bottom) at the centerline, at 1.11 m below the hot-top joint (point P).

of a fixed solid (case 1); there are, however, several differences: (1) the core of the ingot off the centerline is positively segregated, due to the initial enrichment during the creation of the negative bands at the columnar-equiaxed interface; (2) the centerline exhibits a similar segregation profile but less intensive segregation, apart from two peaks in the hot top. These peaks stem from strong local variations in grain density in the hot top at the end of solidification. They affect the solidification kinetics and, in turn, the coupled transport and, thus, the final macrosegregation; (3) the segregations established as a result of the counterclockwise circulation in the packed layer are weaker, due to smaller flow velocities; (4) the A segregates have a somewhat coarser structure and start at a higher position; and (5) the positive hot-top segregation is more intense, due to the grain settling.

C. *Globular Free-Floating Grains*

For case 3, we consider the solidification of the ingot with entirely globular free-floating grains. Already, the final macrosegregation map and centerline profile, shown in Figure 4(c) and Figure 2, respectively, indicate that the settling of solute-lean grains is the dominant phenomenon. The evolution is shown in Figure 10.

The solidification starts with the fast nucleation of the globular grains in the whole ingot, due to the zero superheat. As in the case of dendritic grains, the ingot center is isothermal and the heat transfer is controlled by the solute transport *via* the solidification kinetics. The grains descend next to the columnar front, where the density is higher, and create a vigorous clockwise circulation loop, which evolves into multicellular flow structures (Figure 10(a)). Similar to the case of dendritic grains, the negative segregation bands at the columnar-equiaxed interface are generated at this stage. The globular grains are not entrained by the liquid as strongly as the dendritic grains are, since the ratio of solid volume to surface (and, thus, of buoyancy to drag) is larger. Their sedimentation velocity is, therefore, higher. The grains settling to the bottom descend in a relatively thin layer along the columnar front and are swept toward the center into a horizontal layer of settling grains just above the packed layer. A region in which some grains are entrained upward by the fluid flow is located above this layer, but the flow structure of this region is not stable. In contrast to the dendritic case, the settling of globular grains causes a significant net transport of the solute-lean solid phase downward (compare the evolutions of the liquid fraction in the ingot in Figures 9 and 10). The formation of the strong negative segregation in the sedimentation layer occurs at the moment at which the settling grains are stopped, which is indicated by the grain-transport term of Eq. [A3], which becomes large at the top of the packed layer. The zone above the packed layer, on the contrary, is continuously enriched by the solute-rich liquid that is ejected upward by the settling grains. Due to this continuous enrichment of the top part of the ingot, a strong vertical segregation gradient is created in the segregation induced by the settling. The other fundamental difference from the dendritic ingot of case 2 is that in the globular sedimentation layer there is no significant fluid flow, which was decisive for the macrosegregation formation in the dendritic case. The grains are packed at a solid fraction of $g_s = g_{env} = 0.4$, and the strong hydraulic drag effectively blocks the liquid flow in the packed layer, which now becomes too weak to cause any additional changes in the macrosegregation. This also prevents the formation of mesosegregations.

V. CONCLUSIONS

A multiphase solidification model tackling the motion and growth of equiaxed grains has been presented. The model is able to predict the grain density, grain morphology, and segregation pattern at the end of the solidification. It was used to simulate the casting of a 3.3-ton ingot that was characterized experimentally. We investigated the effects of the motion of dendritic and globular free-floating grains as well as of the natural convection flow on the macrosegregation in the ingot; we used the experimental results as an indication of the validity of the predictions. The computations were performed with finer grids than it was possible to use in previous studies, even when the grain motion was accounted for; thus, more detailed results were obtained. Notably, the improved grid resolution made possible the prediction of the formation of A segregates in the top part of the ingot, in the fixed-solid case. These mesoscale segregation structures were not found with the coarser grids. We analyzed the formation of the most prominent segregation zones, the negative segregation at the bottom, the positive hot-top segregation, and the centerline segregation, by applying a simple analytical criterion (developed in the Appendix). The importance of the heat transfer in the hot top for the formation of the centerline macrosegregation, as discussed previously by Flemings, has been emphasized. Further, we concluded that the strong positive segregation at the top of the ingot cannot be attributed to an enrichment linked to the formation of A segregates, as some previous studies suggested.[34] Rather, we have shown that the enrichment originates from the global circulation of interdendritic liquid. This is further affirmed by the computations on a coarse grid that did not show A segregates, but that still predicted a positive segregation of the same order of magnitude as in the top part of the ingot. The importance of the liquid circulation was shown by a computation with modified thermal and solutal expansion coefficients that resulted in a flow dominated by thermal rather than solutal buoyancy and that showed a completely different segregation pattern.

When taking into account the motion of dendritic free-floating grains, we found the same segregation tendencies as in the case of a fixed solid phase. The analysis of the results showed that the main effect of the settling of dendritic grains was the reduction in the intensity of the flow of the interdendritic liquid in the loosely packed sedimentation layer, due to an increase in the solid fraction and the resulting decrease in the permeability. The flow of interdendritic liquid continues to be the principal phenomenon responsible for the segregation; however, a globally lower segregation intensity results from the weaker flow. When taking into account the motion of globular free-floating grains, on the other hand, the settling of the solute-lean grains into a tightly packed layer becomes the principal phenomenon responsible for the macrosegregation. Due to the high solid fraction in the packed layer, the intensity of the flow of the interdendritic liquid is very weak and cannot significantly modify the macrosegregation; an additional consequence is that no mesosegregations were observed. The comparison of the model predictions with the experimental results revealed that the most significant discrepancies, by far, occurred in the globular case. This shows the importance of the proper modeling of the grain morphology when considering the motion of free-floating grains in steel ingots.

A considerable amount of work remains to be done to determine and quantify the scenario of the formation of the free-floating grains. The most important additional development following this work is the refinement and investigation of the model, in order to describe the morphology transition between dendritic and globular grains.

ACKNOWLEDGMENTS

This work was supported by the research program OSC, which was co-financed by the French research ministry and eight industrial partners (Aubert & Duval, Ascometal, CTIF, Erasteel, Fonderie de l'Atlantique, Industeel, PSA, SCC, and Transvalor), and in part by a consortium of ArcelorMittal, Ascometal, Aubert & Duval, Erasteel, and Rio Tinto Alcan.

APPENDIX

Adding the average solute mass balance in the solid and liquid phases (Eqs. [6] and [7]) and accounting for relation [21], one gets

$$\frac{\partial(\rho_m C_m)}{\partial t} + \nabla(\rho_s g_s C_s \vec{v}_s) + \nabla(\rho_l g_l C_l \vec{v}_l) = 0 \qquad [A1]$$

with $\rho_m C_m = \rho_s g_s C_s + \rho_l g_l C_l$.

By applying mass conservation (Eq. [3]) and assuming equal and constant densities of the solid and liquid phases, Eq. [A1] becomes

$$\frac{\partial(C_m)}{\partial t} = -g_s \vec{v}_s \cdot \nabla(C_s) - g_l \vec{v}_l \cdot \nabla(C_l) - (C_s - C_l) \cdot \nabla(g_s \vec{v}_s) \qquad [A2]$$

Assuming in addition, the local thermodynamic equilibrium in the entire liquid and solid phases (lever rule), the partial time derivative of the average local solute mass fraction can then be expressed as

$$\frac{\partial(C_m)}{\partial t} = \underbrace{-\frac{(g_s k_P \vec{v}_s + g_l \vec{v}_l)}{m_L} \cdot \nabla(T)}_{\text{motioncoupledwithphasechange}} \underbrace{-\left(\frac{\partial(g_s)}{\partial t} - \frac{1}{\rho_s}(\Gamma_s - \Phi_s)\right)(1 - k_P) C_l}_{\text{graintransport}} \qquad [A3]$$

For a negative liquidus slope m_L, the first term of Eq. [A3] means that any motion of the solid and liquid phases, such that the velocity component parallel to the thermal gradient is oriented in the same direction as the thermal gradient, will induce an increase in the average solute mass fraction. At the reverse, if the parallel velocity component is in the direction opposite to the thermal gradient, a decrease in the average solute mass fraction will be observed. The second (grain transport) term quantifies the contribution of the transport of solid grains (purely passive transport, *i.e.*, without phase change) on the average solid mass fraction. Note that this equation allows a direct interpretation of the circulation of the solid and liquid phases on the variation in the local solute content; in the more general case, however, in which shrinkage is accounted for, it is possible to derive only a relation between the relative motion of the phases and the partial derivative of the solute mass fraction of the liquid *vs* the volume fraction of the liquid.[2]

NOMENCLATURE

C^i	concentration of element i
C_d	drag coefficient
D	diffusion coefficient
d_g	equivalent grain diameter
d_s	equivalent solid phase diameter
$\vec{g}$	gravity acceleration
g^{block}	packing grain-volume fraction
g_{env}	grain (dendrite envelope) volume fraction
g_l	liquid volume fraction
g_s	solid volume fraction
g_s^c	grain impingement limit
g_{si}	internal solid fraction
h	specific enthalpy
k	thermal conductivity
K	permeability
k_p^i	partition coefficient for element i
l_1	primary dendrite arm length
m_L^i	liquidus slope for element i
N	grain density (number of grains per unit volume)
P	pressure
Re	Reynolds number
S_{env}	envelope surface area density
S_V	solid-liquid interfacial area density
Sc	Schmidt number
SDAS	secondary dendrite arm spacing
t	time
T	temperature
T_f	melting temperature of pure iron
$\vec{v}$	velocity
V_0	initial grain volume at nucleation
V_{env}	initial grain volume at nucleation
V_{tip}	dendrite tip velocity

GREEK SYMBOLS

β_C^i	solutal expansion coefficient for element i
β_T	thermal expansion coefficient
Γ_{env}	grain (dendrite envelope) growth rate
Γ_s	solid growth rate
δ_l	solute diffusion length in the liquid
δ_s	solute diffusion length in the solid
μ_l	liquid viscosity
ρ	density
ρ_g	density in the buoyancy term
Φ_s	solid mass generation due to nucleation

SUBSCRIPTS AND SUPERSCRIPTS

$_{env}$	grain envelope
$_l$	liquid phase

^{s} solid phase
* equilibrium at the solid-liquid interface

REFERENCES

1. A. Hultgren: *Scand. J. Metall*., 1973, vol. 2, pp. 217–27.
2. M.C. Flemings: *Scand. J. Metall*, 1976, vol. 5, pp. 1–15.
3. R. Mehrabian, M. Keane, and M.C. Flemings: *Metall. Trans*, 1970, vol. 1, pp. 1209–20.
4. Y.-K. Chuang and K. Schwerdtfeger: *Arch. Eisenhüttenwes*, 1975, vol. 46, pp. 303–10.
5. A. Olsson, R. West, and H. Fredriksson: *Scand. J. Metall*, 1986, vol. 15, pp. 104–12.
6. W.D. Bennon and F.P. Incropera: *Int. J. Heat Mass Transfer*, 1987, vol. 30, pp. 2161–70.
7. S. Ganesan and D.R. Poirier: *Metall. Trans. B*, 1990, vol. 21B, pp. 173–81.
8. D.R. Poirier, P.J. Nandapurkar, and S. Ganesan: *Metall. Trans. B*, 1991, vol. 22B, pp. 889–900.
9. J. Ni and C. Beckermann: *Metall. Trans. B*, 1991, vol. 22B, pp. 349–61.
10. I. Ohnaka: in *State of the Art of Computer Simulation of Casting and Solidification Processes*, H. Fredriksson, ed., Les éditions de physique, Les Ulis, France, 1986, pp. 211–23.
11. F. Roch, H. Combeau, J, Chevrier, and G. Lesoult: in *Modeling of Casting, Welding and Advanced Solidification Processes V*, M. Rappaz, M.R. Özgü, and K.W. Mahin, eds., TMS, Warrendale, PA, 1991, pp. 789–96.
12. F. Roch, H. Combeau, I. Poitrault, J. Chevrier, and G. Lesoult: *6th Int. Iron and Steel Congr*., ISIJ, Nagoya, Japan, 1990, pp. 665–72.
13. I. Vannier, H. Combeau, and G. Lesoult: *Numiform '92, 4th International Conference on Numerical Methods in Industrial Forming Processes*, J.-L. Chenot, R.D. Wood, and O.C. Zienkiewicz, eds., Balkema, Rotterdam, 1992, pp. 835–40.
14. I. Vannier, H. Combeau, and G. Lesoult: *Mater. Sci. Eng., A*, 1993, vol. 173, pp. 317–21.
15. J. Common, J. Delorme, and P. Bastien: *Rev. Metall*., 1973, vol. 70 (4), pp. 251–58.
16. J.P. Gu and C. Beckermann: *Metall. Mater. Trans. A*, 1999, vol. 30A, pp. 1357–66.
17. C.Y. Wang and C. Beckermann: *Metall. Mater. Trans. A*, 1996, vol. 27A, pp. 2754–64.
18. B. Appolaire, V. Albert, H. Combeau, and G. Lesoult: *Acta Mater*., 1998, vol. 46, pp. 5851–62.
19. B. Appolaire, V. Albert, H. Combeau, and G. Lesoult: *ISIJ*, 1999, vol. 39, pp. 263–70.
20. A. Badillo, D. Ceynar, and C. Beckermann: *J. Cryst. Growth*, 2007, vol. 309, pp. 197–215.
21. A. Badillo, D. Ceynar, and C. Beckermann: *J. Cryst. Growth*, 2007, vol. 309, pp. 216–24.
22. B. Appolaire and H. Combeau: *Int. Symp. Liquid Metal Processing and Casting*, Ecole des Mines de Nancy, Nancy, France, 2003, pp. 233–39.
23. B. Rabia: Doctoral Thesis, Institut National Polytechnique de Lorraine, Ecole des Mines de Nancy, Nancy, France, 2004.
24. C. Camperola: Ecole des Mines d'Albi, Albi, France, internal note, 2003.
25. I. Vannier: Doctoral Thesis, Institut National Polytechnique de Lorraine, Ecole des Mines de Nancy, Nancy, France, 1995.
26. N. Ahmad, H. Combeau, J.-L. Desbiolles, T. Jalanti, G. Lesoult, J. Rappaz, M. Rappaz, and C. Stomp: *Metall. Mater. Trans. A*, 1998, vol. 29A, pp. 617–30.
27. J. Ni and C. Beckermann: *J. Mater. Process. Manuf. Sci*., 1993, vol. 2, pp. 217–31.
28. S. Charmond: Technical Report, Ecole Nationale Supérieure de Chimie de Clermont-Ferrand, Clermont-Ferrand, France, 2005.
29. S. Charmond: Master's Thesis, Ecole Nationale Supérieure de Chimie de Clermont-Ferrand, Clermont-Ferrand, France, 2006.
30. B. Appolaire, H. Combeau, and G. Lesoult: *Mater. Sci. Eng., A*, 2008, vol. 487, pp. 33–45.
31. W. Kurz, B. Giovanola, and R. Trivedi: *Acta Metall*., 1986, vol. 34, pp. 823–30.
32. M.C. Schneider and C. Beckermann: *Metall. Mater. Trans. A*, 1995, vol. 26A, pp. 2373–87.
33. M. Založnik and B. Šarler: in *Modeling of Casting, Welding and Advanced Solidification Processes XI*, C.-A. Gandin and M. Bellet, eds., TMS, Warrendale, PA, 2006, pp. 243–50.
34. C. Beckermann: *Int. Mater. Rev*., 2002, vol. 47, pp. 243–61.